https://doi.org/10.26565/2220-637X-2025-45-01 ISSN 2220-637X
УДК: 004.94 + 54-145.4 + 544.034.1 + 544.272 + 544.623

LOCAL STRUCTURE AND LI-ION TRANSPORT MECHANISM IN LIFSI/DME/BTFE ELECTROLYTE REVEALED BY MOLECULAR DYNAMICS SIMULATION

K. S. Dikarieva[a,*], V. Koverga[b,†,‡], O. N. Kalugin[c,*]

**Education and Research Institute of Chemistry, V.N. Karazin Kharkiv National University, Kharkiv, Ukraine*
†Department of Chemical Engineering, University of Illinois at Chicago, Chicago, USA
‡Materials Science Division, Argonne National Laboratory, Lemont, USA

a) katerynadikarieva@gmail.com https://orcid.org/0009-0003-4805-4614
b) vkoverga@uic.edu https://orcid.org/0000-0002-6248-7438
c) onkalugin@gmail.com https://orcid.org/0000-0003-3273-9259

Fluorinated ether-based electrolytes represent a promising avenue for improving lithium-ion battery performance and safety, yet the molecular mechanisms governing ion transport in these systems remain insufficiently understood. To elucidate the solvation behavior and ion dynamics in mixed solvents, molecular dynamics simulations of 1M (bisfluorosulfonyl)imide (LiFSI) / 1,2-dimethoxyethane (DME) / bis (2,2,2-trifluoroethyl)ether (BTFE) (1:1) system were performed. The results reveal a distinct solvation preference: Li^+ form predominantly anion-rich aggregates ($FSI_3DME_1BTFE_0$, 28.9%) instead of traditional solvent-separated structures, with fluorinated BTFE completely excluded from the first coordination shell despite its equimolar presence. Diffusion analysis showed significant mobility differences – BTFE diffuses 17-18 times faster than ionic species−while van Hove correlation function demonstrate that Li^+ transport proceeds via hopping between confined regions rather than continuous diffusion. Cluster analysis reveals small weakly charged aggregates dominating the electrolyte structure, explaining the system's efficient charge transport. These molecular insights provide design principles for optimizing fluorinated ether electrolytes with enhanced ionic conductivity.

Keywords: lithium-ion battery electrolytes, molecular dynamics simulation, hopping transport mechanism, ion clustering, fluorinated solvents, solvation shell structure.

Introduction

The development of advanced lithium-based batteries requires electrolytes with wide electrochemical stability windows, high ionic conductivity, thermal stability and compatibility with lithium-metal anodes [1-3]. While carbonate-based electrolytes dominate in current lithium-ion batteries, their limitations – including flammability, poor high-voltage stability and reduced performance at extreme temperatures – motivate the search for safer alternatives [4-6].

Ether-based electrolytes offer promising advantages such as better thermal resistance, lower flammability and excellent compatibility with lithium-metal anodes. Among ether solvents, 1,2- dimethoxyethane (DME) exhibits strong Li^+ solvating capacity due to its bidentate coordination ability [7]. However, pure DME electrolytes suffer from poor oxidative stability and suboptimal transport properties [8, 9], necessitating mixed-solvent formulations with fluorinated co-solvents [10, 11].

Fluorination of ether solvents has emerged as an effective approach to enhance battery performance [12, 13]. Fluorine atoms withdraw electron density, strengthening adjacent bonds and improving oxidative stability while promoting stable solid electrolyte interphase formation [14, 15]. However, the effect is non-linear: moderate fluorination increases ionic conductivity and anodic stability, while excessive substitution can increase viscosity and impair Li^+ solvation [16]. Bis(2,2,2-trifluoroethyl)ether (BTFE), despite lower conductivity than mono- or difluorinated analogues, provides high oxidative stability and reduced flammability [17].

Recent experimental studies of 1M LiFSI/DME/BTFE mixtures demonstrate high ionic conductivity, wide electrochemical windows, and improved interfacial stability [8, 18, 19].

Spectroscopic measurements, including ^{17}O NMR and Raman spectroscopy, confirm BTFE's minimal participation in Li^+ coordination, suggesting its role as a non-coordinating diluent [17, 20]. The choice of LiFSI over conventional salts like $LiPF_6$ is driven by its higher ionic conductivity, superior

thermal stability, and ability to form robust fluorine-rich interphases that synergize with low-coordinating solvent like BTFE [8, 18, 19].

While experimental data provide valuable macroscopic insights, understanding the molecular-level mechanisms governing ion transport and solvation requires computational approaches. Molecular dynamics (MD) simulations enable direct correlation between solvation structure, local organization and transport properties in complex multicomponent systems [21]. Recent MD studies of fluorinated electrolytes have revealed the prevalence of in Li^+ - anion aggregates and weak solvation behavior in system like FEME [16], while multiscale approaches combining MD with DFT have established design principles for fluorinated diethoxyethane variants [22]. However, systematic MD investigation of BTFE-containing LiFSI/DME system remain absent.

This study addresses this gap through comprehensive MD simulations of 1M LiFSI/DME/BTFE (1:1) electrolyte. We examine in Li^+ solvation structures through radial distribution function analysis, evaluate transport properties via diffusion coefficients and van Hove correlation functions, characterize solvation shell composition, and analyze ion clustering behavior. These molecular-level insights provide fundamental understanding and design principle for optimizing fluorinated ether electrolytes for next-generation lithium batteries.

Methodology

Details of molecular dynamics modeling. MD were carried out using LAMMPS (Large-scale Atomic/Molecular Massively Parallel Simulator) package version 08-02-2023, for a ternary LiFSI/DME/BTFE mixture in equimolar ratio (containing 288 molecules of each components), corresponding to a cubic simulation box length of 57.79 Å, respectively [23].

The system sizes were selected to balance computational efficiency with the minimization of finite-size effects, following the rationale of Yeh and Hummer. To account for residual finite-size effects in diffusion coefficients, the Yeh-Hummer correction was applied [24]:

$$D_0 = D + \frac{2.8373 k_B T}{6\pi\eta L} \quad (1)$$

where D is the corrected diffusion coefficient, D_0 is the raw MD value, k_B is the Boltzmann constant, T is the temperature, η is the shear viscosity and L is the box length.

The geometry of the ions and solvent molecules investigated in this work are shown in Figs.1-3.

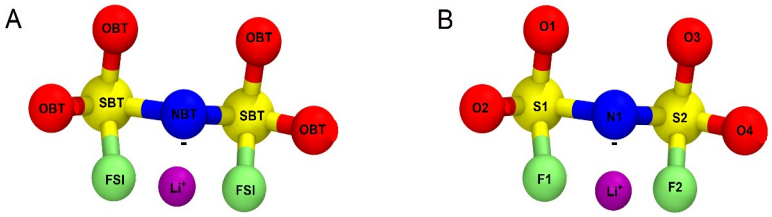

Figure 1. Illustration of lithium cation (Li^+) and bis(fluorosulfonyl)imide (FSI^-, $[N(SO_2F)_2]^-$), which was studied in this work, where (**A**) the accepted acronyms for atom types used in the force field are shown, and (**B**) the atom labeling nomenclature used for structural analysis is presented.

.

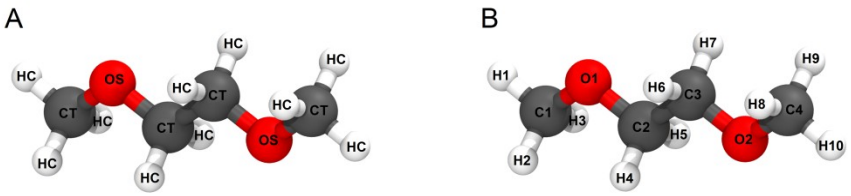

Figure 2. Illustration of 1,2-Dimethoxyethane (DME, $C_4H_{10}O_2$), which was studied in this work, where (**A**) the accepted acronyms for atom types used in the force field are shown, and (**B**) the atom labeling nomenclature used for structural analysis is presented.

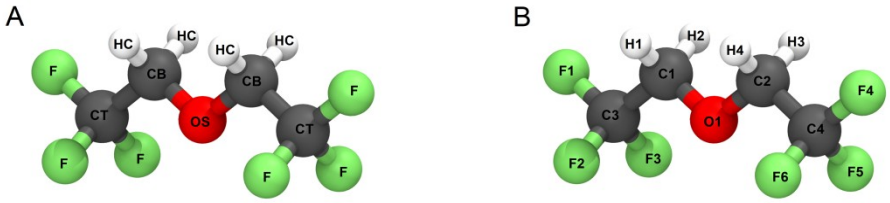

Figure 3. Illustration of bis(2,2,2-trifluoroethyl)ether (BTFE, $C_4H_4F_6O$), which was studied in this work, where (**A**) the accepted acronyms for atom types used in the force field are shown, and (**B**) the atom labeling nomenclature used for structural analysis is presented.

The LiFSI/DME/BTFE ternary system was simulated using the OPLS-AA force field, with parameters generated via LigParGen [25]. For OPLS-AA, harmonic potentials were used for bond stretching and angle bending, while dihedral interactions were describes as a sum of cosine functions up to the fourth harmonic. Scaling factors for 1-4 interactions were set to 0.5, and the Lennard-Jones mixing rules was arithmetic for OPLS-AA. These parameters optimized for liquid-phase systems and ensure correct reproduction of intermolecular interactions in the simulation.

The total potential energy of the system was expressed as [26]:

$$U_{total} = U_{bonded} + U_{nonbonded} \tag{2}$$

where the bonded component comprised bond, angle, dihedral and improper contributions:

$$U_{bonded} = U_{bond} + U_{angles} + U_{dihedrals} + U_{impropers} \tag{3}$$

$$U_{bond} = k_r \left(r - r_0\right)^2 \tag{4}$$

$$U_{angle} = k_\theta \left(\theta - \theta_0\right)^2 \tag{5}$$

$$U_{dihedral} = \frac{k_1}{2}[1+\cos(\phi)] + \frac{k_2}{2}[1-\cos(2\phi)] + \frac{k_3}{2}[1+\cos(3\phi)] + \frac{k_4}{2}[1-\cos(4\phi)] \tag{6}$$

where U_i– potential energy, k_i – force constant, r_i, θ_i and ϕ – associated with degrees of freedom for covalent bonds, angles and dihedral angles.

The non-bonded interactions consisted of Lennard-Jones and Coulomb terms:

$$U_{nonbonded} = \sum_{i>j} 4\varepsilon_{ij}\left[\left(\frac{\sigma_{ij}}{r_{ij}}\right)^{12} - \left(\frac{\sigma_{ij}}{r_{ij}}\right)^{6}\right] + \sum_{i>j}\frac{Cq_iq_j}{\varepsilon r_{ij}} \tag{7}$$

where q_i –partial charge, ε_0 – dielectric constant , r – interatomic distance, ϵ – depth of potential minimum, σ – distance to potential minimum.

Mixing parameters were determined:

$$\varepsilon_{ij} = \sqrt{\varepsilon_{ii}\varepsilon_{jj}}, \quad \sigma_{ij} = \frac{\sigma_{ii} + \sigma_{jj}}{2} \tag{8}$$

where ε_{ij} is Lennard-Jones energy parameter (well depth) between species *i* and *j*, σ_{ij} is Lennard-Jones size parameter (collision diameter) between species *i* and *j*, ε_{ii}, ε_{jj} is Lennard-Jones energy parameters for pure components *i* and *j*, σ_{ii}, σ_{jj} is Lennard-Jones size parameters for pure components *i* and *j*.

Quantum chemical calculations were also carried out for the FSI^- anion and its partial atomic charges were refined using the CHELPG scheme at the MP2/cc-pVTZ level of theory.

The parameters of the inter- and intramolecular interactions are given in Tables 1–8.

Table 1. Intermolecular parameters for the Li^+ and FSI^- represented as partial charges (q), whereas the Lennard-Jones potentials are represented by the distance (σ) to the potential minimum and the depth of the potential well (ε) for the corresponding atoms shown in Figure 1.

Atoms	Atoms type	q / e	ε / kcal mol^{-1}	σ / Å
Li	Li	1.0000	0.018	2.13
N1	NBT	0.0122	0.170	3.25
S1	SBT	0.4746	0.250	3.55
S2				
O1		-0.3488		
O2	OBT	-0.3488	0.170	2.96
O3		-0.3488		
O4		-0.3488		
F1	FSI	-0.2831	0.060	2.90
F2		-0.2831		

Table 2. Intramolecular stretching and bending parameters for the Li^+ and FSI^- corresponding to the relevant degrees of freedom, taken from the OPLS-AA library (see the figure corresponding atomic labels, Figure 1).

Bonds	r_0 /Å	k_r / kcal mol^{-1} Å^{-2}
FSI-SBT	1.60	336.92
SBT-OBT	1.44	700.00
SBT-NBT	1.67	434.00
Angles	θ_0 / °	k_θ / kcal mol^{-1} rad^{-2}
FSI-SBT-OBT	104.36	78.67
FSI-SBT-NBT	104.36	78.67
OBT-SBT-NBT	107.00	120.00
SBT-NBT-SBT	118.33	48.37
OBT-SBT-OBT	119.00	104.00

Table 3. Intermolecular parameters for DME represented as partial charges (q), whereas the Lennard-Jones potentials are represented by the distance (σ) to the potential minimum and the depth of the potential well (ε) for the corresponding atoms shown in Figure 2.

Atoms	Atoms type	q / e	ε / kcal mol^{-1}	σ / Å
C1		-0.0600		
C2	CT	-0.0126	0.066	3.50
C3		-0.0126		
C4		-0.0600		
O1	OS	-0.3645	0.140	2.90
O2		-0.3644		
H1		0.0843		
H2		0.0843		
H3		0.0843		
H4	HC	0.0920	0.030	2.50
H5		0.0920		
H6		0.0920		
H7		0.0920		
H8		0.0844		
H9		0.0844		
H10		0.0844		

Table 4. Intramolecular stretching and bending parameters for DME corresponding to the relevant degrees of freedom, taken from the OPLS-AA library (see the figure corresponding atomic labels, Figure 2).

Bonds	r_0 /Å	k_r / kcal mol^{-1} Å^{-2}
CT-HC	1.090	340
CT-OS	1.410	320
CT-CT	1.529	268
Angles	θ_0 / °	k_θ / kcal mol^{-1} rad^{-2}
HC-CT-HC	107.8	33.0
HC-CT-OS	109.5	35.0
CT-OS-CT	109.5	60.0
CT-CT-OS	109.5	50.0
HC-CT-CT	110.7	37.5

Table 5. Dihedral angle potential parameters for DME corresponding to the relevant degrees of freedom, taken from the OPLS-AA library (see the figure with corresponding atomic labels, Figure 2.)

Dihedral	k_1 / kcal mol^{-1}	k_2 /kcal mol^{-1}	k_3 /kcal mol^{-1}	k_4 /kcal mol^{-1}
HC-CT-OS-CT	0.00	0.00	0.76	0.00
CT-OS-CT-CT	0.65	-0.25	0.67	0.00
OS-CT-CT-OS	-0.55	0.00	0.00	0.00
HC-CT-CT-HC	0.00	0.00	0.30	0.00
HC-CT-CT-OS	0.00	0.00	0.468	0.00

Table 6. Intermolecular parameters for BTFE, represented as partial charges (q), whereas the Lennard-Jones potentials are represented by the distance (σ) to the potential minimum and the depth of the potential well (ε) for the corresponding atoms shown in Figure 3.

Atoms	Atoms type	q / e	ε / kcal mol^{-1}	σ / Å
O1	OS	-0.3421	0.140	2.90
C1		-0.0688		
C2	CT	-0.0691	0.066	3.50
C3		0.4557		
C4	CB	0.4557	0.030	2.50
H1		0.1220	0.030	2.50
H2	HC	0.1220		
H3		0.1219		
H4		0.1219		
F1		-0.1533		
F2		-0.1533		
F3		-0.1533	0.060	2.90
F4	F	-0.1531		
F5		-0.1531		
F6		-0.1531		

Table 7. Intramolecular stretching and bending parameters for BTFE corresponding to the relevant degrees of freedom, taken from the OPLS-AA library (see the figure corresponding atomic labels, Figure 3).

Bonds	r_0 /Å	k_r / kcal mol^{-1} Å^{-2}
CB-F	1.360	367
CB-CT	1.529	268
CT-OS	1.410	320
CT-HC	1.090	340

Angles	θ_0 / °	k_θ / kcal mol^{-1} rad^{-2}
F-CB-F	109.10	77.0
F-CB-CT	109.5	50.0
CB-CT-OS	109.5	50.0
CT-OS-CT	109.5	60.0
CB-CT-HC	110.7	37.5
HC-CT-OS	109.5	35.0
HC-CT-HC	107.8	33.0

Table 8. Dihedral angle potential parameters for BTFE corresponding to the relevant degrees of freedom, taken from the OPLS-AA library (see the figure with corresponding atomic labels, Figure 3)

Dihedral	k_1 / kcal mol^{-1}	k_2 /kcal mol^{-1}	k_3 /kcal mol^{-1}	k_4 /kcal mol^{-1}
OS-CT-CB-F	0.00	0.00	0.54	0.00
CB-CT-OS-CT	0.65	-0.25	0.67	0.00
HC-CT-CB-F	0.00	0.00	0.36	0.00
HC-CT-OS-CT	0.00	0.00	0.76	0.00

Non-bonded interactions were computed with a cutoff of 12 Å for both Lennard-Jones and Coulombic terms, applying long-range electrostatics via the particle-particle particle-mesh (PPPM) method. The neighbor list was updated with 2 Å and long-range dispersion corrections were applied to ensure accurate pressure and energy evaluation.

Prior to the production phase, each system underwent energy minimization using the steepest descent algorithm until one of the following convergence criteria was met: (i) change in total energy below $1\cdot10^{-4}$ kcal·mol^{-1} per step, (ii) maximum atomic force below $1\cdot10^{-6}$ kcal·mol^{-1} Å^{-1}, or (iii) 500,000 iterations.

Equations of motion were integrated using the velocity-Verlet algorithm with a timestep of 0.5 fs. This short timestep was required to accurately resolve high-frequency vibrational modes, particularly in hydrogen-containing bonds, while maintaining numerical stability [27]. System equilibration was performed for 10 ns in the *NPT* ensemble at T = 298 K and p = 1 atm, regulated by the Nosé-Hoover thermostat and barostat [28-31], each with a relaxation time of 0.3 ps and 0.8 ps, respectively. The barostat relaxation time was set to 0.8 ps to allow gradual pressure adjustment while maintaining numerical, whereas the thermostat relaxation time was set to 0.3 ps to efficiently control temperature without perturbing high-frequency vibrations. This was followed by a 10 ns *NVT* production run using the same thermostat settings. Equilibration was verified by monitoring convergence of total, potential and kinetic energies, as well as temperature, pressure and density to time-independent averages.

To characterize the studied systems, we focused on key structural and dynamic properties. Structural properties were analyzed through radial distribution function (*RDFs*), cluster analysis and solvation shell characterization.

Pair radial distribution functions

$$g(r) = \frac{1}{N}\sum_{i=1}^{N}\frac{1}{4\pi r_{ij}^{\,2}\Delta r}\delta\left(r - r_{ij}\right) \tag{9}$$

where N, r_{ij}, and Δr represent the total number of atoms within a radius r, the distance between atoms i and j, and the bin width, respectively were calculated using the TRAVIS "TRajectory analyzer and VISualizer" v1.14.0 package [32].

Cluster analysis and solvation shell characterization were conducted using the solvation analysis [33] in conjunction with Python scripts, providing insight into Li^+ coordination environments and solvation structures.

Translational dynamics were analyzed through mean-squared displacement (*MSD*) calculations. The *MSD*, representing the average squared displacement of molecules from their initial positions, was computed as[34]:

$$MSD = \frac{1}{N}\sum_{i=1}^{N}\left|\boldsymbol{r}(t) - \boldsymbol{r}(0)\right|^2 = \Delta\left|\boldsymbol{r}(t)\right|^2 \tag{10}$$

where N is the number of particles, $r(t)$ is the centre of mass coordinate of the particle *i* at the time *t,* and $\langle\cdot\rangle$ denotes an ensemble average over time.

Self-diffusion coefficients D_i were derived from *MSD* data using Einstein's relation:

$$D_i = \frac{1}{6}\lim_{t\to\infty}\frac{d}{dt}\left(\boldsymbol{r}(t)-\boldsymbol{r}(0)\right)^2 \tag{11}$$

The temporal dependence of diffusive behavior was characterized through the logarithmic slope of *MSD*:

$$\beta(t) = \frac{d\ \log\mathrm{MSD}(t)}{d\log t} \tag{12}$$

This parameter distinguishes the nature of diffusion: $\beta = 1$ corresponds to the diffusion regime (Fickian transport), $\beta < 1$ indicate sub-diffusive behavior, and $\beta > 1$ signifies super-diffusive or ballistic motion at short timescales.

Microscopic transport mechanisms were elucidated through van Hove correlation function analysis, describing space-time correlations between species [35]:

$$G(r,t) = \frac{1}{4\pi\rho N r^2}\sum_{i,j}\delta(r-\left|\mathrm{r}_i(0)-\mathrm{r}_j(t)\right|) \tag{13}$$

where ρ is atom number density, r is the distance. Next, van Hove function was decomposed by two parts – *self*:

$$G^{self}(r,t) = \frac{1}{4\pi\rho N r^2}\sum_{i}\delta(r-\left|\mathrm{r}_j(t)\right|) \tag{14}$$

and *distinct*:

$$G^{distinct}(r,t) = \frac{1}{4\pi\rho N r^2}\sum_{i}\delta(r-\left|\mathrm{r}_i(0)-\mathrm{r}_j(t)\right|) \tag{15}$$

The detailed characterization of structural and dynamic properties provided a comprehensive foundation for evaluating the LiFSI/DME/BTFE system, and the following section presents the results and discussion of the simulations.

Results and Discussion

Li^+ Solvation Structure and Coordination Environment in the LiFSI/DME/BTFE Electrolyte

To understand the solvation structure of LiFSI salt in the DME/BTFE electrolyte system and its influence on the Li^+ transport mechanism, the radial distribution between representative atomic centers of all electrolyte components was analyzed (Figure 4).

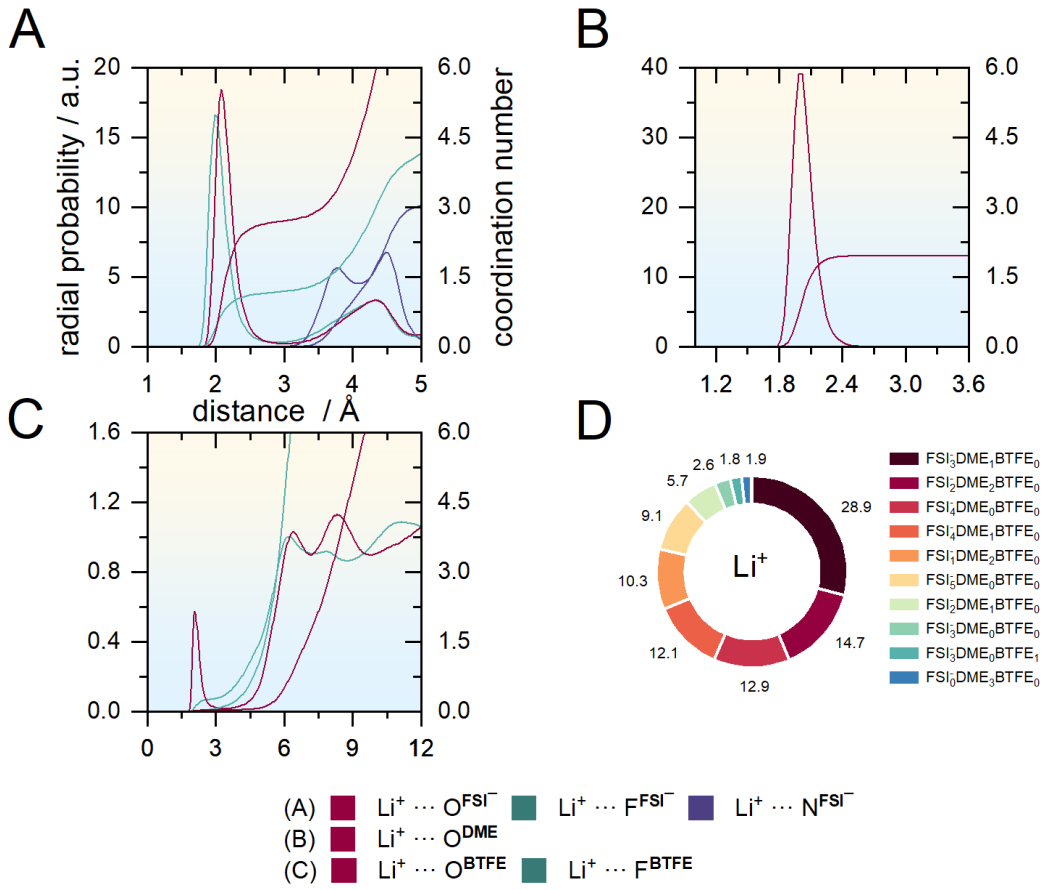

Figure 4. Li^+ solvation structure in the LiFSI/DME/BTFE electrolyte (1 M LiFSI in DME/BTFE = 1:1) illustrated by (**A–C**) radial distribution functions (*g(r)*, left axis) and running coordination numbers (*cn(r)*, right axis) for (**A**) $Li^+\cdots FSI^-$, (**B**) $Li^+\cdots$BTFE, and (**C**) $Li^+\cdots$DME interactions. (**D**) Statistical distribution of the Li^+ coordination environment, determined using a cut-off distance of 3.00 Å defining the first solvation shell.

A detailed investigation of the $Li^+\cdots FSI^-$ interionic interactions (Figure 4a), for which the oxygen atom is the strongest interaction center in FSI^-, revealed a pronounced peak at ≈ 2.1 Å with a mini- mum at 3 Å. This indicates relatively strong interionic interactions that are typical for liquid organic electrolytes and ionic liquids containing lithium salts with imide anions. Li^+ also demonstrates competitive solvation by DME molecules. The first peak for $Li^+\cdots O^{DME}$ (Figure 4b) (1.9 Å) appears at a somewhat shorter distance than for $Li^+\cdots O^{FSI}$, indicating a strong tendency for Li^+ localization with DME and higher interaction strength. In contrast to DME and FSI^-, the radial distribution functions for $Li^+\cdots$ BTFE (Figure 4c) exhibit only a shallow, broad maximum at $r \approx 2.1$ Å with $g(r) < 0.8$, followed by a diffuse minimum near $r \approx 3.6$ Å. The extent of the solvation shell for different pairs differs more sub - stantially than their interaction strength. The minimum in the radial distribution for FSI^- is located at 3 Å, whereas for DME it is at 2.5 Å, which is explained by the higher coordination capacity of DME to Li^+ due to the stronger donor ability of the ether groups. For BTFE, the minimum at ≈ 3.6 Å confirms the absence of significant direct interaction. Although no substantial first-shell coordination is ob - served for BTFE [8, 36], a minor long-range correlation peak is present at $r > 4$ Å, indicating an indi- rect influence of BTFE on the spatial organization of the electrolyte. These features suggest that BTFE influences the spatial organization of DME and FSI^- indirectly, modulating the local solvation land- scape without forming stable complexes with Li^+. Such behavior aligns with the solvation-structure regulation hypothesis proposed for fluorinated co-solvents in ether-based electrolytes [37].

The analysis of the position, intensity, and shape of radial distributions describing interactions between electrolyte components is reflected in the running coordination number *cn*(*r*), which represents the coordination capacity of the reference atom with respect to Li^+ ions and was calculated by integrating the distribution up to the first minimum (right Y-axis of Figure 4). The coordination number for $Li^+\cdots O^{FSI}$ is ≈1.43, indicating a multidentate binding configuration of FSI^-, where each anion provides more than one oxygen atom for Li^+ coordination. The coordination number for $Li^+\cdots O^{DME}$ is ≈1.7, which is significantly

lower compared to DME-rich systems ($n \approx 3.0–5.0$) and is consistent with the reduced availability of coordinating DME molecules in the equimolar DME/BTFE mixture. For $Li^+\cdots$BTFE, integration yields coordination numbers close to zero, confirming the absence of significant direct Li^+–BTFE interactions. When combining contributions from FSI^- and DME, the total coordination number reaches approximately 3.5, indicating a solvation shell partially dominated by the anion.

For a more detailed investigation of the role of each component as a coordination center within the LiFSI/DME/BTFE electrolyte system, a statistical analysis of the Li^+ coordination environment was performed (Figure 4d). Each configuration was designated with an X-Y-Z label corresponding to the number of FSI^-, DME, and BTFE, respectively, in the first solvation shell (3.00 Å). Specifically, for the local Li^+ environment, the most prevalent configuration is $FSI_3DME_1BTFE_0$ (28.9%), reflecting a strong tendency toward anion-rich solvation, where three FSI^- molecules surround Li^+ together with one DME molecule. Several other FSI^--rich motifs also appear with significant frequency: $FSI_2DME_2BTFE_0$ (14.7%) and $FSI_4DME_1BTFE_0$ (12.9%), forming the second and third most populated environments. Together, these states reinforce the picture of extensive ion pairing, as Li^+ is rarely coordinated with fewer than two anions in the system. Interestingly, only one configuration – $FSI_3DME_1BTFE_1$ – includes BTFE directly in the coordination sphere, and even then its frequency remains minimal, emphasizing the negligible coordinating capacity of BTFE. This tendency underscores the competition between anion association and solvation by DME molecules. The predominant presence of multi-anion aggregates reflects strong ion-pairing interactions, indicating that Li^+ in this electrolyte exists predominantly in highly associated states. This defines the ion transport mechanism in the LiFSI/DME/BTFE system, where Li^+ transport occurs predominantly through mixed solvation complexes $Li^+(FSI^-)_n(DME)_m$ with dominant participation of FSI^-, while BTFE serves as a diluent that influences the structural organization of the electrolyte indirectly, without forming direct coordination bonds with Li^+.

Ion cluster population analysis in LiFSI/BTFE/DME system

The analysis of ionic cluster formation can additionally shed light on the Li^+ transport mechanism in the LiFSI/DME/BTFE electrolyte through understanding how the identified solvation complexes organize into larger ionic aggregates and how this organization affects ionic transport dynamics.

The population analysis of ionic cluster formation is presented in Fig. 5 as a two-dimensional distribution of the number of FSI^- anions as a function of the number of Li^+ cations in each cluster. The probability map, plotted on a logarithmic scale, visualizes the distribution of ionic aggregates in the electrolyte. A key feature of the distribution is the evident predominance of small ionic clusters. The highest occurrence frequencies are concentrated in the region where both n^+ and n^- do not exceed approximately 5, indicating that most ions exist as small, highly dynamic aggregates rather than large cluster structures.

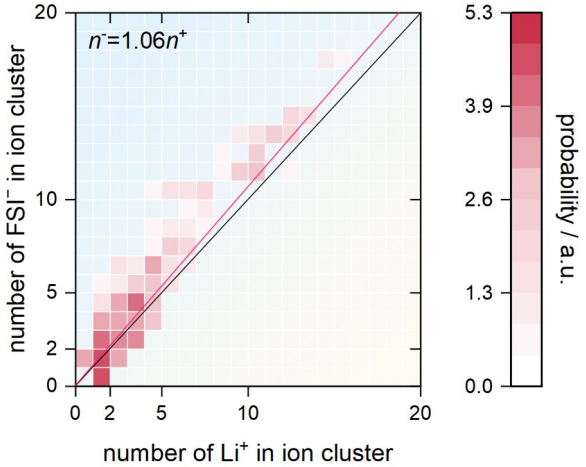

Figure 5. Ion cluster population analysis of FSI^- with respect to Li^+ in the LiFSI/BTFE/DME electrolyte, represented on a logarithmic probability scale. The color map indicates the occurrence frequency of the corresponding $Li^+\cdots FSI^-$ clusters identified along the simulation trajectory. The black diagonal line denotes electrically neutral aggregates ($n^- = n^+$), while the red line, obtained from a first-degree polynomial fit ($n^- = 1.06 \cdot n^+$), indicates a deviation from neutrality toward negatively charged, anion-rich clusters (1.06 > 1). Cluster analysis was performed using a threshold distance criterion between Li^+ and the N/O/F interaction centers of FSI^-.

The black diagonal line in the figure corresponds to the electroneutrality condition ($n^- = n^+$). The data distribution follows this neutrality line with a high degree of accuracy, demonstrating that the overwhelming majority of clusters remain charge-balanced. The linear fit, shown in red, yields a relationship of $n^- = 1.06 \cdot n^+$, indicating a slight deviation from ideal neutrality. The coefficient exceeding unity by only 6% indicates a weak enrichment of clusters with FSI^- anions, suggesting a somewhat higher propensity of anions for association compared to Li^+ cations. However, this deviation is minimal and does not lead to a substantial change in the overall neutral character of the ionic aggregates.

The dominance of small, near-neutral clusters defines the nature of the ionic transport mechanism in the LiFSI/DME/BTFE electrolyte. Although the coordination environment analysis revealed the predominance of highly associated solvation complexes $Li^+(FSI^-)_3(DME)_1$, the cluster population analysis demonstrates that these local complexes do not combine into extended ionic networks. In contrast to high-salt-concentration systems where the formation of large higher-order aggregates is observed, this system exhibits limited aggregation. The main contribution comes from free Li^+ ions and small neutral pairs, while the formation of large aggregates ($n^+ + n^- > 10$) is virtually absent. This phenomenon is due to the effective solvation of both ion types by DME and BTFE solvent molecules, which prevent excessive ionic association at the mesoscopic level.

The weak anion enrichment of clusters ($n^- = 1.06 \cdot n^+$) correlates with the coordination environment analysis results, where mixed solvation complexes with an FSI^- /DME ratio of ≈ 3:1 are dominant. This quantitative agreement between the local coordination structure and cluster distribution confirms that the observed solvation complexes $Li^+(FSI^-)_n(DME)_m$ represent the primary transport units, which remain relatively isolated and do not form extensive cluster domains. Li^+ cations are preferentially coordinated by oxygen-containing groups of DME, which promotes stabilization of solvation complexes and prevents their further aggregation. Meanwhile, FSI^- anions demonstrate a somewhat higher tendency to form weak associates, which is reflected in the minimal excess of anions in the clusters.

The results of the ionic cluster population analysis combined with coordination environment data provide compelling evidence that Li^+ transport in the LiFSI/DME/BTFE electrolyte occurs predominantly through a vehicular mechanism involving small solvation complexes, rather than through structural diffusion in extended cluster domains. The nanoscale structural organization of the electrolyte is characterized by the predominance of small, weakly associated ionic species. The minimal formation of large charged aggregates ensures high mobility of Li^+ charge carriers, as the ions remain in the form of discrete solvation complexes $Li^+(FSI^-)_n(DME)_m$ and are not bound in extended cluster domains. Charge transport occurs through diffusion of these solvated complexes as unified transport units, which ensures efficient ionic transport while maintaining the dynamic nature of the solvation shell. The role of BTFE as a diluent is to create spatial separation between solvation complexes, preventing their aggregation and maintaining high mobility of the transport units.

The structural characteristics of clusters reflect only the static aspect of ionic organization; to complement the analysis with a dynamic component and determine the nature of ion motion on different time scales, Van Hove function analysis is subsequently applied.

Space-time Analysis of Li^+ Transport via the Van Hove Correlation Functions

To quantitatively characterize dynamics of Li^+ transport and confirm the proposed transport mechanism, Van Hove function analysis was performed, which allows tracking the evolution of ion distribution over time and determining the characteristic scales of ionic transport.

The analysis of the self-correlation part of the Van Hove function, representing the temporal evolution of the probability of individual Li^+ ion displacement relative to its initial position, is presented in Figure 6A. The probability distribution of Li^+ displacement demonstrates characteristic temporal evolution. At short time intervals (dark purple curves, 0–$3 \cdot 10^6$ fs), the distribution is characterized by a pronounced sharp peak at small distances (~1–2 Å) with a maximum displacement probability of approximately 178 arbitrary units, indicating predominantly localized ion motion within their first coordination shell. As the observation time increases (transition from purple to red and yellow curves), the intensity of the main peak decreases and its maximum shifts to larger distances, reaching ~ 2–3 Å at times ~ 8–$10 \cdot 10^6$ fs. Simultaneously, an extended tail of the distribution forms, extending to 6–8 Å, indicating the realization of long-range ion displacements.

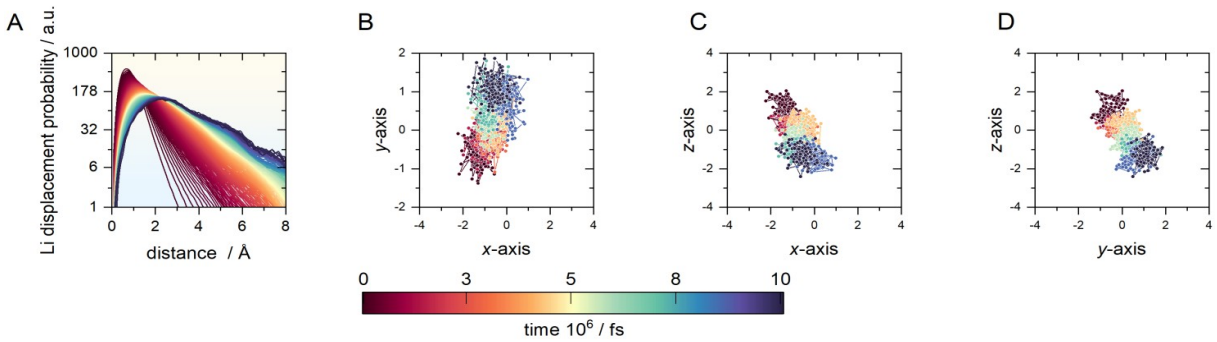

Figure 6. Illustration of Li^+ transport dynamics in the 1 M LiFSI BTFE/DME (1:1) electrolyte. (**A**) Self-part of the van Hove correlation function describing the probability distribution of individual Li^+ displacements over time. (**B–D**) Two-dimensional projections of a representative single Li^+ trajectory in the (**B**) *xy*-, (**C**) *xz*-, and (**D**) *yz*-planes. Color coding indicates the simulation time (fs), highlighting the temporal evolution and spatial confinement of Li^+ motion along the trajectory.

A more detailed investigation of the distribution shape reveals characteristic features of the transport mechanism. In contrast to continuous diffusive motion, where the distribution would have a Gaussian form, the observed distribution demonstrates pronounced asymmetry with a long tail toward larger distances. This indicates that Li^+ transport occurs not through continuous diffusion but through intermittent motion with alternating periods of localization and relatively rapid jumps (hopping-type mechanism). Li^+ ions remain localized within a certain coordination environment for significant time intervals, after which discrete jumps occur over distances of 6–8 Å, corresponding to transition to a new solvation state.

For a more detailed understanding of the spatial organization of Li^+ trajectories, Fig. 6B-D present two-dimensional projections of an individual cation trajectory in the *xy*, *xz*, and *yz* planes, respectively, with color coding by simulation time. The trajectories demonstrate an intermittent character with the formation of discrete spatial clusters. By focusing on the displacement of a single arbitrary cation rather than on averaged characteristics, the heterogeneity of dynamics can be more clearly revealed. The color coding (from dark blue for early times through yellow to red for late stages) visualizes the sequence of positions occupied by the ion. In all three projections, the formation of spatially separated clusters of points of the same color is observed, indicating that the ion spends significant time in limited local regions (~2–3 Å) before moving to the next localized region. Transitions between such regions occur as jumps over distances of ~4–6 Å.

The observed behavior indicates a predominantly hopping transport mechanism. During localization periods, the ion performs limited oscillatory motion within ~2 Å. The dominant contribution to long-range transport is made by jumps between localized regions, which occur through overcoming an energy barrier. This process is realized as activated hops, which explains the intermittent character of the trajectories and the presence of a long tail in the Van Hove function distribution.

Thus, the totality of Van Hove function data convincingly demonstrates that Li^+ transport in the LiFSI/DME/BTFE electrolyte is realized predominantly through a hopping mechanism (structural diffusion). Ions reside in local solvation environments for discrete time intervals, after which they perform activated hops to new coordination positions. Long-range transport occurs through a series of such hops over distances of 4–8 Å, which ensures efficient Li^+ movement through the electrolyte.

Diffusive Behavior and Transport Properties of LiFSI/DME/BTFE Electrolyte

Numerical assessment of the mobility of all system components was performed through calculation of self-diffusion coefficients based on mean square displacement (*MSD*). For quantitative assessment of diffusion, self-diffusion coefficients were determined from the slope of the mean square displacement (*MSD*) curves of each component in the long-time diffusive regime (Fig. 7).

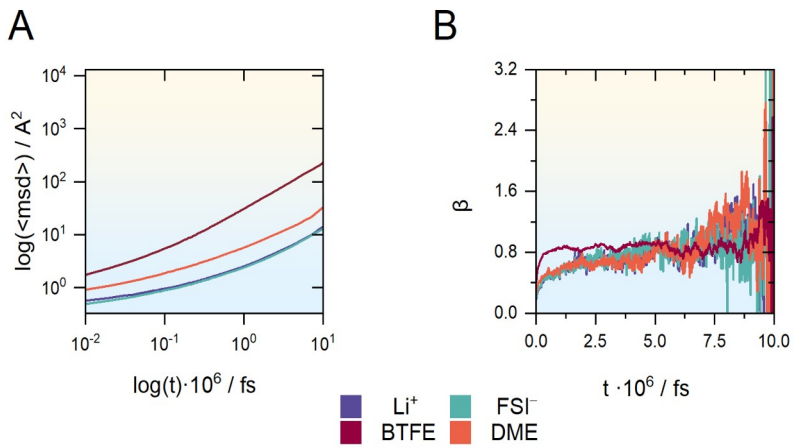

Figure 7. Illustration of transport of electrolyte constituents, represented by (**A**) mean-squared displacement and (**B**) time evolution of β parameter quantifying diffusion behavior.

Figure 7A shows the mean square displacement of all components on a logarithmic scale, where the linear behavior in the long-time regime confirms diffusive motion. In this approach, the slope of the *MSD* curves provides a direct measure of particle mobility. The calculation of *D* was carried out in the time range between 4 and 7 ps, where the system reaches the diffusive regime. In this time range, the coefficient β, characterizing the type of diffusive motion, reaches a value close to 1, as shown in Figure 7B, confirming the establishment of a linear diffusive regime for all electrolyte components. The convergence of β to unity for all species at times beyond 4–7 ps indicates the transition from ballistic to diffusive regime.

The self-diffusion coefficients of all major components − Li^+, DME, BTFE, and FSI^- − were extracted from the *MSD* analysis, and the results are presented in Table 10.

Table 10. The self-diffusion coefficients of the electrolyte 1M LiFSI DME/BTFE (1:1) constituents.

Component systems	Self-diffusion coefficient $(D)\cdot 10^{12}$/ m²/s
Li^+	2.00
FSI^-	1.98
DME	4.22
BTFE	35.30

The obtained data demonstrate that neutral co-solvent molecules (BTFE) diffuse significantly faster than ionic species. The observed mobility order is BTFE > DME > $Li^+ \approx FSI^-$. Specifically, BTFE exhibits the highest self-diffusion coefficient, approximately 17–18 times higher than the ion coefficients, which is likely due to weak interactions with Li^+ and exclusion from the first solvation shell, as established in the *RDF* analysis. DME diffuses approximately twice as fast as Li^+ or FSI^-, reflecting its role as a coordinating solvent participating in the formation of solvation complexes.

Analysis of the data presented in Figure 4 allows establishing a direct connection between the structural features of the system revealed in the RDF and coordination environment analysis and its dynamic behavior. Li^+ and FSI^- exhibit the lowest diffusion coefficients, consistent with strong ionic association and partially anion-dominated solvation revealed in the coordination environment analysis.

Conclusions

Molecular dynamics simulations of the 1M LiFSI/DME/BTFE (1:1) electrolyte revealed a unique solvation structure characterized by the predominance of anion-enriched aggregates. The most prevalent Li^+ coordination configuration, $FSI_3DME_1BTFE_0$ (28.9%), demonstrates that BTFE is completely excluded from the first solvation shell ($cn \approx 0$) and functions as a non-coordinating diluent. Cluster population analysis confirms the dominance of small, weakly charged aggregates

($n^- = 1.06 \cdot n^+, n^+ + n^- < 5$), preventing the formation of extended ionic networks.

Li^+ transport in this electrolyte proceeds predominantly via a hopping mechanism with alternating periods of localization (~2 Å) and activated jumps over distances of 4 – 8 Å. Van Hove function analysis revealed the intermittent nature of motion with solvation shell reorganization. Nearly identical diffusion coefficients for Li^+ ($2.00 \cdot 10^{-12}$ m²/s) and FSI^- ($1.98 \cdot 10^{-12}$ m²/s) indicate persistent ion pairing, while BTFE exhibits 17 – 18 times higher mobility due to the absence of coordination interactions.

The obtained results establish design principles for fluorinated ether electrolytes: spatial dilution by non-coordinating solvents prevents excessive ionic aggregation while ensuring efficient charge transport through small dynamic solvation complexes. The identified hopping mechanism with low reorganization barriers, enabled by small cluster size, provides a foundation for optimizing high-voltage lithium batteries.

Acknowledgements

The authors are grateful to the Ministry of Education and Science of Ukraine for financial support within the framework of basic funding. Computer calculations were performed using the computing resource *Dell EMC PowerEdge R740 supercomputer* of the Center for Collective Use of Scientific Equipment "*Laboratory of Micro- and Nano-Systems, New Materials and Technologies*" of the Ministry of Education and Science of Ukraine at the V.N. Karazin Kharkiv National University and also *Azzurra* HPC *center*, Université Côte d'Azur, Nice, France. Additional computational resources were provided by the *Bebop* high-performance computing cluster operated by the Laboratory Computing Resource Center at Argonne National Laboratory.

Conflict of Interest: The authors declare no conflict of interest

Authors Contributions: All authors have contributed equally to this work.

References

1. Wang, H., et al., *Liquid electrolyte: The nexus of practical lithium metal batteries.* Joule, 2022. **6**(3): p. 588-616. https://doi.org/10.1016/j.joule.2021.12.018
2. Zhou, J., et al., *Advanced Liquid Electrolyte Design for High-Voltage and High-Safety Lithium Metal Batteries.* Advanced Energy Materials, 2025. **15**(34): p. 2502654. https://doi.org/10.1002/aenm.202502654
3. Zhang, J.-G., et al., *Lithium Metal Anodes with Nonaqueous Electrolytes.* Chemical Reviews, 2020. **120**(24): p. 13312-13348. https://doi.org/10.1021/acs.chemrev.0c00275
4. Tan, S., et al., *Review on Low-Temperature Electrolytes for Lithium-Ion and Lithium Metal Batteries.* Electrochemical Energy Reviews, 2023. **6**(1): p. 35. https://doi.org/10.1007/s41918-023-00199-1
5. Liu, J., et al., *Pathways for practical high-energy long-cycling lithium metal batteries.* Nature Energy, 2019. **4**(3): p. 180-186. https://doi.org/10.1038/s41560-019-0338-x
6. Deng, K., et al., *Nonflammable organic electrolytes for high-safety lithium-ion batteries.* Energy Storage Materials, 2020. **32**: p. 425-447. https://doi.org/10.1016/j.ensm.2020.07.018
7. Yu, Z., et al., *Rational solvent molecule tuning for high-performance lithium metal battery electrolytes.* Nature Energy, 2022. **7**(1): p. 94-106. https://doi.org/10.1038/s41560-021-00962-y
8. Holoubek, J., et al., *Electrolyte Design Implications of Ion-Pairing in Low-Temperature Li Metal Batteries.* Energy & Environmental Science, 2022. **15**(12): p. 4969-4981. https://doi.org/10.1039/D1EE03422G
9. Zhao, Y., et al., *Electrolyte engineering via ether solvent fluorination for developing stable non-aqueous lithium metal batteries.* Nature Communications, 2023. **14**(1): p. 299. https://doi.org/10.1038/s41467-023-35934-1
10. Cao, X., et al., *Effects of fluorinated solvents on electrolyte solvation structures and electrode/electrolyte interphases for lithium metal batteries.* Proceedings of the National Academy of Sciences, 2021. **118**: p. e2020357118. https://doi.org/10.1073/pnas.2020357118
11. Tran, T.N., et al., *Enhancing Cycling Stability of Lithium Metal Batteries by a Bifunctional Fluorinated Ether.* Advanced Functional Materials, 2024. **34**(42): p. 2407012. https://doi.org/10.1002/adfm.202407012
12. Chen, S., et al., *High-Efficiency Lithium Metal Batteries with Fire-Retardant Electrolytes.* Joule, 2018. **2**(8): p. 1548-1558. https://doi.org/10.1016/j.joule.2018.05.002

13. Li, X., et al., *Weakly Solvating Electrolytes for Lithium and Post -Lithium Rechargeable Batteries: Progress and Outlook.* Advanced Energy Materials, 2025. 15(25): p. 2501272. https://doi.org/10.1002/aenm.202501272
14. Xiang, J. and Y.-C. Lu, *Ether-Based High-Voltage Lithium Metal Batteries: The Road to Commercialization.* ACS Nano, 2024. **18**(16): p. 10726-10737. https://doi.org/10.1021/acsnano.4c00110
15. He, S., et al., *A self-assembly capsule-like solvation structure electrolyte for lithium metal batteries.* Materials Today Energy, 2025. **48**: p. 101759. https://doi.org/10.1016/j.mtener.2024.101759
16. Hasan, R. and D. Datta, *Computational Study of Li+ Solvation Structures in Fluorinated Ether, Non-Fluorinated Ether, and Organic Carbonate-Based Electrolytes at Low and High Salt Concentrations* , 2025. **4**: p. 1049-1066. https://doi.org/10.1039/D5YA00154D
17. Li, G.-X., et al., *Enhancing lithium-metal battery longevity through minimized coordinating diluent.* Nature Energy, 2024. **9**: p. 1-11. https://doi.org/10.1038/s41560-024-01519-5
18. Han, H.-B., et al., *Lithium bis(fluorosulfonyl)imide (LiFSI) as conducting salt for nonaqueous liquid electrolytes for lithium-ion batteries: Physicochemical and electrochemical properties.* Journal of Power Sources, 2011. **196**(7): p. 3623-3632. https://doi.org/10.1016/j.jpowsour.2010.12.040
19. Schweigart, P., et al., *On the Viability of Lithium Bis(fluorosulfonyl)imide as Electrolyte Salt for Use in Lithium-Ion Capacitors.* Batteries & Supercaps, 2023. **6**(9): p. e202300226. https://doi.org/10.1002/batt.202300226
20. Zhang, G., et al., *A bifunctional fluorinated ether co-solvent for dendrite-free and long-term lithium metal batteries.* Nano Energy, 2022. **95**: p. 107014. https://doi.org/10.1016/j.nanoen.2022.107014
21. Yu, Z., et al., *Simulation Guided Molecular Design of Hydrofluoroether Solvent for High Energy Batteries.* Journal of Materials Chemistry A, 2024. **12**(10): p. 6294-6301. https://doi.org/10.1039/D3TA07670A
22. Yuan, X., et al., *Design principles of fluoroether solvents for lithium metal battery electrolytes unveiled by extensive molecular simulation and machine learning.* Journal of Energy Chemistry, 2025. **102**: p. 52-62. https://doi.org/10.1016/j.jechem.2024.10.021
23. Thompson, A.P., et al., *LAMMPS - a flexible simulation tool for particle-based materials modeling at the atomic, meso, and continuum scales.* Computer Physics Communications, 2022. **271**: p. 108171. https://doi.org/10.1016/j.cpc.2021.108171
24. Yeh, I.-C. and G. Hummer, *System-Size Dependence of Diffusion Coefficients and Viscosities from Molecular Dynamics Simulations with Periodic Boundary Conditions.* The Journal of Physical Chemistry B, 2004. **108**(40): p. 15873-15879. https://doi.org/10.1021/jp0477147
25. Dodda, L.S., et al., *LigParGen web server: an automatic OPLS-AA parameter generator for organic ligands.* Nucleic Acids Research, 2017. **45**(W1): p. W331-W336. https://doi.org/10.1093/nar/gkx312
26. Hou, T., et al., *The Solvation Structure, Transport Properties and Reduction Behavior of Carbonate-Based Electrolytes of Lithium-Ion Batteries.* Chemical Science, 2021. **12**(44): p. 14740-14751. https://doi.org/10.1039/D1SC04265C
27. Asthagiri, D.N. and T.L. Beck, *MD Simulation of Water Using a Rigid Body Description Requires a Small Time Step to Ensure Equipartition.* Journal of Chemical Theory and Computation, 2024. **20**(1): p. 368-374. https://doi.org/10.1021/acs.jctc.3c01153
28. Nosé, S., *A unified formulation of the constant temperature molecular dynamics methods.* The Journal of Chemical Physics, 1984. **81**(1): p. 511-519. https://doi.org/10.1063/1.447334
29. Hoover, W., *Canonical Dynamics: Equilibrium Phase-Space Distributions.* Phys. Rev. A: At., Mol., Opt. Phys., 1985. **31**: p. 1695. https://doi.org/10.1103/PhysRevA.31.1695
30. Martyna, G.J., D.J. Tobias, and M.L. Klein, *Constant pressure molecular dynamics algorithms.* The Journal of Chemical Physics, 1994. **101**(5): p. 4177-4189. https://doi.org/10.1063/1.467468
31. Martyna, G.J., M.L. Klein, and M. Tuckerman, *Nosé–Hoover chains: The canonical ensemble via continuous dynamics.* The Journal of Chemical Physics, 1992. **97**(4): p. 2635-2643.
32. Brehm, M. and B. Kirchner, *TRAVIS - A Free Analyzer and Visualizer for Monte Carlo and Molecular Dynamics Trajectories.* Journal of Chemical Information and Modeling, 2011. **51**(8): p. 2007-2023. https://doi.org/10.1021/ci200217w

33. Cohen, O., et al., *SolvationAnalysis: A Python toolkit for understanding liquid solvation structure in classical molecular dynamics simulations.* Journal of Open Source Software, 2023. **8**: p. 5183. https://doi.org/10.21105/joss.05183
34. Maginn, E.J., et al., *Best Practices for Computing Transport Properties 1. Self-Diffusivity and Viscosity from Equilibrium Molecular Dynamics [Article v1.0].* Living Journal of Computational Molecular Science, 2018. **1**(1): p. 6324. https://doi.org/10.33011/livecoms.1.1.6324
35. Hansen, J.-P. and I. McDonald, *Theory of Simple Liquids: With Applications to Soft Matter: Fourth Edition.* Theory of Simple Liquids: With Applications to Soft Matter: Fourth Edition, 2013, Oxford: Academic Press. 636.
36. Jiang, L.-L., et al., *Inhibiting Solvent Co-Intercalation in a Graphite Anode by a Localized High-Concentration Electrolyte in Fast-Charging Batteries.* Angewandte Chemie International Edition, 2020. **60**: p.1-6. https://doi.org/10.1002/anie.202009738
37. Li, G.X., et al., *Fine-Tuning Li-Ion Solvation Structure by Enhanced Solvent-Diluent Interactions for Long-Cycling Lithium Metal Batteries.* Advanced Energy Materials, 2025. **15**: p. 2405680. https://doi.org/10.1002/aenm.202405680

Received 11.09.2025 *Accepted 23.10.2025* *Published 30.12.2025*

К. С. Дікарєва[*], В. Коверга[†‡], О. М. Калугін[*]. Локальна структура та механізм транспорту Li^+ в електроліті LiFSI/DME/BTFE за даними молекулярно-динамічного моделювання.

[*] Навчально-науковий інститут Хімії, Харківський національний університет імені В. Н. Каразіна, Харків, Україна
[†] Кафедра хімічної інженерії, Університет Іллінойсу в Чикаго, Чикаго, США
[‡] Відділ матеріалознавства, Національна лабораторія Аргонн, Лемонт, США

Фторовані етерні електроліти є перспективним напрямом для підвищення ефективності та безпечності літієвих акумуляторів, однак молекулярні механізми, що визначають транспорт Li^+ у таких системах, досі недостатньо зрозумілі. З метою з'ясування сольватаційної структури було проведено моделювання методом молекулярної динаміки електроліту 1 M LiFSI у суміші 1,2-диметоксиетану (DME) та біс(2,2,2-трифлуороетил)етеру (BTFE) у співвідношенні 1:1.

Отримані результати показують сольватаційну специфічність: йони Li^+ переважно формують аніон-насичені агрегати типу $FSI_3DME_1BTFE_0$ (28.9%), а не класичні структури з розділенням розчинників; при цьому фторований BTFE повністю витіснений із першої координаційної сфери, попри рівні молярні кількості у системі. Аналіз дифузії демонструє суттєвий контраст у дифузійній здатності компонентів − BTFE рухається у 17–18 разів швидше за йонні види. Кореляційна функція Ван Хофа показує, що перенесення Li^+ реалізується не шляхом безперервної дифузії, а через стрибки між локалізованими областями.

Кластерний аналіз свідчить, що структуру електроліту визначають невеликі, слабкозаряджені агрегати, що узгоджується з ефективним перенесенням заряду в системі. Отримані на молекулярному рівні дані формують принципи раціонального дизайну фторованих етерних електролітів із покращеною йонною провідністю.

Ключові слова: *електроліти для літій-іонних акумуляторів, молекулярно-динамічне моделювання, стрибковий механізм транспорту, кластеризація йонів, фторовані етери, сольватаційна структура.*

Конфлікт інтересів: *Автори повідомляють про відсутність конфлікту інтересів.*

Внесок авторів: *Всі автори зробили рівний внесок у цю роботу.*

Надіслано до редакції 11.09.2025 *Прийнято до друку 23.10.2025* *Опубліковано 30.12.2025*